doi.org/10.1002/batt.201900131


# Surface and Interfacial Chemistry in the Nickel-Rich Cathode Materials

Junhyeok Kim,[a] Hyungyeon Cha,[a] Hyomyung Lee,[a] Pilgun Oh,*[b] and Jaephil Cho*[a]

With increasing demands for high energy lithium-ion batteries, layered nickel-rich cathode materials have been considered as the most promising candidate due to their high reversible capacity and low cost. Although some of the materials with nickel contents ≦60% were commercialized, there are tremendous obstacles for further improvement of electrochemical performance, which is strongly related to the unstable cathode surface and interfacial properties. In this regard, a specific review on the interfacial chemistry between the cathode and electrolyte during electrochemical testing is provided. We highlight the underpinning interfacial chemistry and degradation mechanisms of the cathode materials. Finally, light is shed on the recent efforts for enhancing the interfacial stability of the nickel-rich cathode materials.

## 1. Introduction

With extending the applications of the lithium-ion batteries (LIBs) from the mobile electronics to the electric vehicle and electrical energy storage systems, state-of-the-art LIBs with high energy/power density and thermal stability are required.[1–3] To meet these demands, the layered nickel-rich cathode materials have been considered as the most feasible candidate among a variety of the cathode materials owing to their high reversible capacity.[4–7] In particular, the nickel-rich cathodes with the reversible capacity of ~220 mAh $g^{-1}$ delivered higher gravimetric energy density of ~800 Wh $kg^{-1}$ than the conventional $LiCoO_2$ cathode with that of ~570 Wh $kg^{-1}$.[8–9] However, the similar ionic radius between the divalent nickel ions (0.69 Å) and lithium ions (0.76 Å) gave rise to the formation of the NiO-like structure during the electrochemical test because of the Li/Ni disordering.[10] The phase transformation from the layered to the NiO-like structure inhibited the lithium-ion transport at the cathode surface, accelerating the capacity fading.[11–13] Moreover, the anisotropic volume changes of the primary particles in the conventional nickel-rich cathodes with aggregated particle shape can induce the intragranular cracking formation inside the cathode after the prolonged electrochemical test.[14–15] Along the void space that was created by the cracking evolution, the electrolyte could be penetrated, thus leading to the deleterious side reactions with the electrolyte as well as the phase transformation.[16]

Furthermore, having noticed that the electrochemical reaction occurred at the interface between the cathode and electrolyte, we should consider how the damaged cathode can influence the electrolyte during the electrochemical cycling. The dynamic behavior of the cathode-electrolyte interface is described in Figure 1a. In general, the conventional organic electrolyte is not electrochemically decomposed within the cathodic voltage window.[17–18] The nucleophilic reactions between the cathode and electrolyte originated from the spontaneous transition metal reductions.[17–20] This eventually results in the oxidative decompositions of the electrolyte solvent, which creates the organic solid–electrolyte interphase (SEI) layer on the cathode surface. Interestingly, the cathode itself was also subjected to the structural transformation from the layered to the rock-salt like structure because of the reductions of the nickel ions (Figure 1b).[12–13] In addition, the decomposition of the $LiPF_6$ salt in the electrolyte that were widely used in the LIBs could form the inorganic SEI layer and

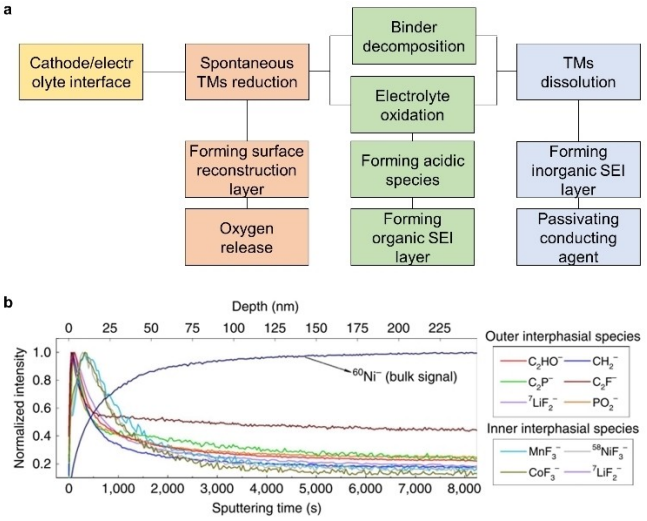


**Figure 1.** Evolution of dynamic interphases between nickel-rich cathodes and electrolyte: (**a**) Evolution mechanisms of the cathode–electrolyte interphases during the battery cycling. (**b**) ToF-SIMS depth profile at the surface of the cycled $LiNi_{0.7}Co_{0.15}Mn_{0.15}O_2$. Part **b** was reproduced with permission of Ref. [28]. Copyright 2017, Macmillan Publisher Limited.

[a] *Dr. J. Kim, H. Cha, H. Lee, Prof. J. Cho*
*Department of Energy Engineering and School of Energy and Chemical Engineering,*
*Ulsan National Institute of Science and Technology (UNIST),*
*44919, Ulsan (Republic of Korea)*
*E-mail: jpcho@unist.ac.kr*
[b] *Prof. P. Oh*
*Department of Graphic Arts Information Engineering*
*Pukyong National University*
*485471, Busan (Republic of Korea)*
*E-mail: poh@pknu.ac.kr*

acidic species such as the hydrofluoric acid (HF) in the presence of the water ($LiPF_6 \rightarrow LiF + PF_5$, $PF_5 + H_2O \rightarrow POF_3 + 2HF$).[21–23] More seriously, the HF is likely to dissolve the transition metal ions in the cathode structure, and the transition metal ions were deposited on the anode side, deteriorating both cathode and anode integrity.[24–29] With respect to the microstructure of the cathode SEI layer, the organic species locally existed at the surface of the interphases; for comparison, the inorganic compounds were distributed inside the interphases (Figure 1c). Even though the solid-state lithium-ion diffusion in the cathode host structure is the rate-determining step during the electrochemical reaction, the cathode SEI layer is closely associated with the charge transfer reaction.[9] Hence, it is highly desired to understand the deleterious side reactions of the cathodes with the electrolyte and their effects on the battery performance. On the basis of such understanding, it is further necessary to rationally design the nickel-rich cathode materials for achieving high energy density.

To mitigate the cathode reactivity with the electrolyte, there are five approaches for the development of high energy LIBs: (1) the incorporation of electrochemically inactive elements into the cathode structure,[30–37] (2) the introduction of the concentration gradient, (3) the introduction of surface coating layer on the cathode,[38–56] (4) the morphological changes to the porous structure, and (5) the crystallinity tuning from the polycrystalline to the single crystalline cathode.[57–66] With respect to the first approach, it could improve the interfacial stability by inhibiting the transition metal reductions. Furthermore, the nickel-rich cathodes with the concentration gradient could also enhance the interfacial stability by mitigating the micro-crack formations during the electrochemical test.

Accordingly, many researchers have intensively concentrated on the surface coating method to physically block the exposed cathode particle against the electrolyte. Although the surface coating layer on the cathode stabilized the interfacial structure, the continuous intragranular cracking evolution caused the exposure of the active primary particle to the electrolyte after the prolonged electrochemical test. In this regard, to entirely accomplish the interfacial stability, there is an increasing volume in the research regarding the single crystalline nickel-rich cathode materials. The single crystalline characteristics could enable the cathode materials to maintain the original morphology because of the isotropic volume changes of the single particle during the charging and discharging process.[67] This morphological integrity could give rise to the formation of the cathode SEI layer at only cathode surface, leading to long-term cycling stability. To date, there have been a variety of the review articles which addressed the complex material and interfacial chemistry.[67–80] Along with the previously published review articles, this review will be of particular interest to the battery researchers who are interested in the interfacial chemistry of the nickel-rich cathode materials.

Herein, we intensively identified the unstable interface between the nickel-rich cathode materials and electrolyte. In section 2, we will detailly cover complex interfacial chemistry between the cathodes and electrolyte, and highlight its effect on the battery degradation and safety. In the final section, a wide range of strategies were intensively investigated for enhancing the interfacial stability of the cathode materials.

## 2. Surface and Interfacial Chemistry

### 2.1. Spontaneous Transition Metals Reduction

The energy difference between the Fermi level ($E_F$) of the cathode and highest occupied molecular orbital (HOMO)/lowest unoccupied molecular orbital (LUMO) of the electrolyte is an important parameter to determine the electrochemical stability of the cathode materials.[81–82] When the $E_F$ of the cathode is close to the HOMO and LUMO of the electrolyte, it gives rise to the oxidation and reduction of the electrolyte,

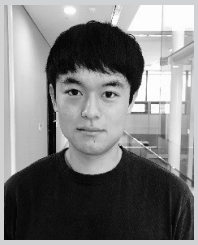

Junhyeok Kim is currently a postdoc in School of Energy Engineering at Ulsan National Institute of Science and Technology (UNIST, Republic of Korea). He received his Ph.D. degree in School of Energy Engineering at UNIST, B.S. degree in Energy and Chemical Engineering from UNIST in 2015. His research interests include the development and investigation of the layered cathode materials for high energy Li-ion batteries.

Pilgun Oh is a professor in department of graphic arts information engineering at Pukyong National University (Republic of Korea). He recieved his Ph.D degree at UNIST under supervison of Prof. Jaephil Cho in 2015. He performed the postdoctoral study at the University of Texas at Austin (USA). His current research is focused on structural charaterization and material modification methods of cathode materials for Li-ion and all-solid state Li-ion batteries.

Jaephil Cho is a professor of School of Energy and Chemical Engineering at UNIST (Republic of Korea). He was a member of Presidential Advisory Council on Science & Technology and a director of the Green Energy Materials Developed Center (granted by Ministry of trade, industry, and energy), and Samsung SDI-UNIST Future Battery Research Center. His current research is focused mainly on Li-ion, all-solid state Li-ion, metal-air, and redox flow batteries for energy storage.

respectively, forming the SEI layer on the cathode. Hence, the energy separation between HOMO and LUMO of the electrolyte provides the potential window for the battery operations. Figure 2a shows the HOMO and LUMO levels of conventional organic electrolyte. The energy levels of the electrolyte were calculated using the density of function theory (DFT) calculations.[83–89] Considering that the conventional nickel-rich cathode materials have been generally operated in the voltage ranged from 2.8 to 4.4 V, there is no thermodynamic driving force about electrolyte electro-decompositions. However, to date, many researchers have observed that the cathode SEI layer was formed even after the electrochemical test or the contact with the electrolyte because of the electro-oxidation of the electrolyte.[13,90–91] For example, Saito et al. intensively investigated the evolution of the SEI layer on the $LiNi_{0.80}Co_{0.15}Al_{0.05}O_2$ (NCA) cathode after the immersion into the electrolyte for 90 days through attenuated total reflectance (ATR) analysis (Figure 2b).[90] The immersed NCA cathode exhibited characteristics IR band peak at 1019 $cm^{-1}$ compared to the pristine NCA, indicating that the P=O bond based materials were formed by the reactions with the electrolyte. More recently, Cherkashinin et al. probed that the $E_F$ of the cathode materials was changed only after contact with the electrolyte.[92] When the cathodes were exposed to the electrolyte, the shift of $E_F$ of the cathodes in relation to the HOMO of the electrolyte solvent induced the oxidative decompositions of the electrolyte solvent because the transition metal was reduced. Actually, their vicinity in the energy levels caused the formation of thin cathode SEI layer with the thickness of ~30 Å.

Aside from the formation of surface film, the changes of local electronic structure in the cathode could give rise to the structural transformation of the cathode. Lin et al. discovered that the phase transition of the $LiNi_{0.4}Mn_{0.4}Co_{0.18}Ti_{0.02}O_2$ cathode when the cathode was exposed to the electrolyte (Figure 2d and **e**).[13] In general, the divalent nickel ions preferentially formed the cation mixing layer over the cobalt and manganese ions because of similar ionic radius of the divalent nickel ions with the lithium ions.[9] Thus, this result indicated that spontaneous reductions of the nickel ions among transition metal ions (from the trivalent nickel ions to the divalent nickel ions) caused the formation of surface reconstruction layer, considerably increasing the charge transfer resistance.

More seriously, the local electronic structure of the cathode was highly evolved during charging process.[18,92] Figure 2f presents the valence band structure in $LiNi_{0.2}Co_{0.7}Mn_{0.1}O_2$ cathode as a function of state of charge (SOC). As increasing the SOC, the overall valence band was strongly modified. Considering that the valence band structure is strongly related with the surface composition, the evolution of the valence band structure was ascribed to the formation of surface layer consisting of organic species during charging process.[92] Furthermore, only divalent nickel ions existed at all SOC state, which implies that the trivalent and tetravalent nickel ions were spontaneously reduced to the divalent nickel ions due to the Jahn-Teller distortions in tri- and tetra-valent nickel ions (Figure 2g).[93–94] The spontaneous transition metal reductions gave rise to the phase transition, which was accompanied by the oxygen containing species such as $O_2$, $O_2^-$, and $O^-$.[94–96] These species could easily react with the electrolyte and accelerate the thermal runaway of the battery, strongly threatening the battery safety.[95,97–102]

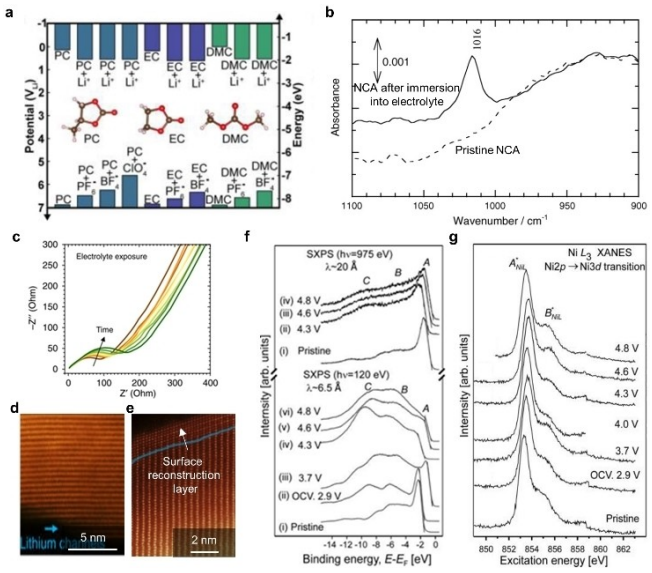


**Figure 2.** Local electronic structure changes of the cathode structure: (**a**) Reduction and oxidation energy level of the conventional electrolyte solvent in the LIBs. Reproduced with permission of Ref. [18]. Copyright 2015, American Chemical Society. (**b**) ATR spectra of the pristine NCA electrode and the NCA electrode after immersion in the electrolyte for 90 days. Reproduced with permission of Ref. [81] Copyright 2007, Elsevier. (**c**) Electrochemical impedance spectroscopy (EIS) results of the $LiNi_{0.4}Mn_{0.4}Co_{0.18}Ti_{0.02}O_2$ cathode with increasing ageing time in the electrolyte. High angle annular dark field scanning transmission electron microscopy (HAADF-STEM) images of (**d**) the pristine $LiNi_{0.4}Mn_{0.4}Co_{0.18}Ti_{0.02}O_2$ cathode and (**e**) the $LiNi_{0.4}Mn_{0.4}Co_{0.18}Ti_{0.02}O_2$ cathode after the electrolyte exposure for 30 h. Part **c**–**e** were reproduced with permission of Ref. [13]. Copyright 2014, Macmillan Publisher Limited. (**f**) Soft X-ray photoemission spectroscopy (SXPS) spectra of the valence band of the $LiNi_{0.2}Co_{0.7}Mn_{0.1}O_2$ cathode as the function of the charging voltage. (**g**) The X-ray absorption near edge structure (XANES) spectra of the $LiNi_{0.2}Co_{0.7}Mn_{0.1}O_2$ cathode as the function of the charging voltage. Part **f** and **g** were reproduced with permission of Ref. [91]. Copyright 2015, American Chemical Society.

### 2.2. Binder and Electrolyte Decomposition

As discussed earlier, the interfacial reactions between the nickel-rich cathode and electrolyte originated from the spontaneous reductions of the transition metal ions. The reduction of the transition metal ions facilitated the catalytic decompositions of the electrolyte solvent, creating the organic SEI layer consisting of carboxylate (O-C=O) and semi carbonates ($ROCO_2Li$) as shown in Figure 3a.[18,23,103–106] The decompositions of the electrolyte solvent were accompanied by the gas generation such as $CO_2$, CO, and $C_xH_y$.[103,107–111] Furthermore, it has been reported that the decompositions of the solvent were enhanced with increasing the temperature.[105,112] Shikano et al. analyzed the formation of organic SEI layer in the $LiNi_{0.73}Co_{0.17}Al_{0.10}O_2$ cathode after the electrochemical test at different temperatures.[105] With increasing the temperatures, the intensity of the organic SEI layer components such as semi-

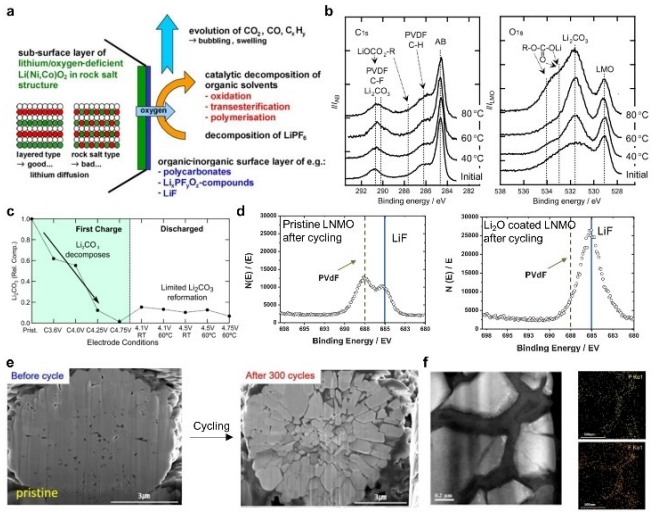


**Figure 3.** Formation of the cathode SEI layer: (**a**) A Schematic illustrating the dynamic behavior of the cathode–electrolyte interface. Reproduced with permission of Ref. [103]. Copyright 2005, Elsevier. (**b**) $C_{1s}$ and $O_{1s}$ high-resolution hard X-ray photoemission spectroscopy (HX-PES) spectra of the $LiNi_{0.73}Co_{0.17}Al_{0.10}O_2$ cathode before and after the electrochemical test with increasing temperature from the room temperature to 80 °C, indicating the formation of organic compounds at the cathode surface. Reproduced with permission of Ref. [105]. Copyright 2007, Elsevier. (**c**) Relative amounts of the $Li_2CO_3$ in the $LiNi_{0.8}Co_{0.15}Al_{0.05}O_2$ cathode during first charging and discharging process with different temperature and voltage. Reproduced with permission of Ref. [112]. Copyright 2018, American Chemical Society. (**d**) X-ray photoemission spectroscopy (XPS) spectra of the pristine LNM and $Li_2O$ coated LNM cathode after 100 cycles at the room temperature. Reproduced with permission of Ref. [119]. Copyright 2014, The Electrochemical Society. (**e**) HAADF-STEM images of the NCM622 cathode before and after the electrochemical test, revealing that the severe micro-cracks were generated inside the cathode particle. (**f**) Energy dispersive X-ray spectroscopy (EDX) mapping results of the NCM622 after 300 cycles at 60 °C. Part **e** and **f** were reproduced with permission of Ref. [40]. Copyright 2015, American Chemical Society.

carbonate and poly-carbonates type compounds significantly increased (Figure 3b). In particular, the lithium carbonate and carbonate containing organic compounds substantially increased at the temperature over 60 °C, suggesting that the catalytic decompositions of the electrolyte solvent were facilitated at the temperature $\geq$ 60 °C.

Along with the electrolyte solvent, the $LiPF_6$ salt in the electrolyte was also decomposed under the presence of moisture during battery cycling, forming the LiF and HF.[113] The LiF on the cathode materials tend to hinder the lithium-ion migration.[114] Furthermore, the oxygen species that were formed by the phase transition of the nickel-rich cathodes could react with the $LiPF_6$ salt, which forms the $Li_xPF_yO_z$ type compound.[17–18] Recently, Lebens-Higgins et al. demonstrated that the decomposition of the $LiPF_6$ salt exhibited strong correlation with the battery operation temperature.[112] They found that the by-products formed by the $LiPF_6$ breakdown existed at the room temperature above 4.25 V, however, the thermal aggravation strongly promoted the salt decompositions at the lower voltage.

With respect to the residual lithium compounds, they were formed by the spontaneous reduction of the trivalent nickel ions to the divalent nickel ions. It has been observed that the residual lithium compounds could react with the $LiPF_6$ salt or residual HF, resulting in the formation of P–O–F bond containing compounds and LiF species.[17,115–116] Such decompositions of the residual lithium compounds were highly facilitated as increasing the charge cut-off voltage in the cell (Figure 3c).[112] After first charge, the small amount of the $Li_2CO_3$ was reformed during the discharge process. To date, the detailed mechanisms regarding the reformation of the $Li_2CO_3$ have not been clearly revealed. However, the existence of the $Li_2CO_3$ on the cathode results in the sluggish kinetics for the lithium ions and electrochemical reaction heterogeneity during the electrochemical test.[110,117] In addition, the residual lithium compounds could react with the PVdF during electrochemical cycling, which results in the LiF formation.[26,118–119] Recently, Cho et al. investigated the correlations between the PVdF binder and residual lithium compounds in the $LiNi_{0.7}Mn_{0.3}O_2$ (LNM) cathode by artificially coating the lithium oxide ($Li_2O$).[119] During air storage, the $Li_2O$ coated LNMO cathode exhibited significant increase of the residual lithium compounds compared to the pristine LNM. These unstable surface properties gave rise to the severe capacity fading in the $Li_2O$ coated LNM cathode. After the electrochemical test, all PVdF binder were decomposed into the LiF in the $Li_2O$ coated LNM cathode; for comparison, the decomposition reactions were mitigated in the pristine LNM (Figure 3d). The progressive formation of the LiF layer on the cathode could block the lithium-ion diffusions and deteriorates the electrochemical performance.

The anisotropic volume changes of each primary particle in the nickel-rich cathode materials could induce the micro-crack generation inside the cathode particles, facilitating the penetration of the electrolyte into the crack.[11,14] The newly exposed primary particles could continuously react with the penetrated electrolyte, which forms the cathode SEI layer at the cracked site.[16,40] Figure 3d shows the morphologies of the $LiNi_{0.6}Co_{0.2}Mn_{0.2}O_2$ (NCM622) cathode before and after the electrochemical test. After 300 cycles at 60 °C, the NCM622 exhibited severe micro-crack evolutions at overall cathode particle. Upon close examination of the cycled cathode, the cathode SEI layer was formed at the cracked site where the lithium-ion transport was severely deteriorated (Figure 3e). Moreover, the degree of the micro-crack evolution exhibited strong dependence on the state of charge (SOC) of the cathode. As increasing the SOC in the cell, the micro-crack was severely generated inside the cathode particle.[16,120] This was ascribed to the increase of the amounts of the extracted lithium ions, causing large volume changes of each primary particle. More seriously, the penetration of the electrolyte into the cracked site was accompanied by the structural transformation of the cathode from the layered to the rock-salt like structure.[16] As discussed earlier, these unstable structural characteristics originated from the spontaneous reductions of the nickel ions (from the tri/tetravalent to the divalent nickel ions).

### 2.3. Transition Metal Dissolution

The acidic species such as the HF that was formed by the decompositions of the $LiPF_6$ salt and PVdF binder could dissolve the transition metal ions in the cathode structure.[25–26,51,121–122] To date, it has been known that the trivalent manganese ions among the transition metal ions were preferentially dissolved from the cathode, which was attributed to the structural instability of the manganese ions.[17,123–128] The Jahn-teller distortions of the trivalent manganese ions gave rise to the disproportionation reactions ($2Mn^{3+} \rightarrow Mn^{2+} + Mn^{4+}$), and the divalent manganese ions were extracted from the cathode.[129–132] Li et al. clearly discovered that a variety of compounds were created at the surface of the $LiNi_{0.61}Co_{0.12}Mn_{0.27}O_2$ cathode after long-term cycling.[29] After 3,000 cycles at room temperature, the acidic species significantly dissolved the transition metal ions as well as the lithium ions at the cathode surface where the lithium fluoride and manganese fluoride were formed (Figure 4a). Furthermore, the intensity of these fluoride compounds increased with increasing cycle number as shown in Figure 4b. The unwanted fluoride containing compounds could degrade the battery performance because such compounds impede the charge transfer reactions at the cathode surface.[114,133]

Furthermore, the dissolved transition metal ions could also degrade the conducting material such as the carbon black in the electrode, lowering the electronic conductivity of the electrode.[28,134] The passivation of the conducting agent originated from the mutual exchange of surface species such as the transition metal fluoride between the cathode and conducting agent. More seriously, this phenomenon occurred when the electrode was only exposed to the electrolyte and was highly evolved during the electrochemical test. Li et al. demonstrated that dynamic behavior of the cathode–electrolyte interface through region-of-interest sensitive secondary ion mass spectroscopy (SIMS).[28] When the electrode was immersed in the electrolyte for 30 days, the intensity of the $C_2F$ and $COF_3$ compounds increased compared with pristine electrode as presented in Figure 4c. The surface species responsible for $C_2F$ and $COF_3$ could be formed by (1) direct HF attack at the conducting agent or (2) acidic species attack at carbonated based electrolyte. Interestingly, such compounds were also observed at the cathode surface, indicating that the fluorine containing organic compounds such as $C_2F$ and $COF_3$ were migrated from the conducting agent to the cathode surface. In addition, when the amount of conducting agent was reduced from 10 wt.% to 1 wt.%, the intensity of the organic compounds in the cathode particle decreased, which reveals that the fluorine containing organic compounds were mainly created from the direct attack of acidic species at the conducting agent. In terms of the metal fluoride compounds, it was also evident that the active mass dissolution product such as LiF and $MnF_2$ were also migrated from the cathode towards carbon–binder interface regions. It is noteworthy that the intensity of the metal fluoride compounds was larger in the electrode with 10 wt.% of the conducting agent than that with 1 wt.% of the conducting agent. This result apparently implied that the conducting agent with larger surface area than the nickel-rich cathode served as an efficient HF scavenger compared to the cathode materials. Hence, it is essential to consider the cathode surface microstructure in combination with the proper electrode design for achieving outstanding electrochemical performance.

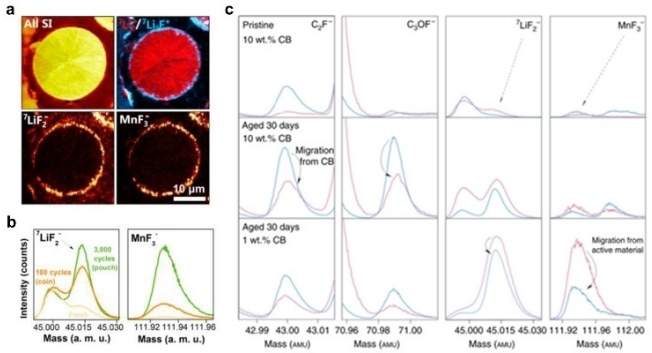


**Figure 4.** Passivation of the cathode electrode by transition metal dissolution: (**a**) Illustrative ToF-SIMS chemical mapping results of the $^7Li^{2+}$, $^7Li_2F^+$, $^7LiF_2^-$, $MnF_3^-$ on the $LiNi_{0.61}Co_{0.12}Mn_{0.27}O_2$ cathode after 3,000 cycles at the room temperature. (**b**) ToF-SIMS spectra of the $^7LiF_2^-$ and $MnF_3^-$ fragments after 100 cycles and 3,000 cycles at the room temperature. Part a and b were reproduced with permission of Ref. [29]. Copyright 2017, American Chemical Society. (**c**) ToF-SIMS spectra collected from the pristine $LiNi_{0.61}Co_{0.12}Mn_{0.27}O_2$ cathode (10 wt.% carbon black) and the 30-days aged $LiNi_{0.61}Co_{0.12}Mn_{0.27}O_2$ cathode (1 wt.% and 10 wt.% carbon black), implying the mutual exchanges of the organic and inorganic compounds between the cathode and carbon black. Reproduced with permission of Ref. [28]. Copyright 2017, Macmillan Publisher Limited.

Aside from the degradation of the cathode and conducting agent, the dissolved transition metal ions from the cathode could deteriorate anode integrity. It has been known that the transition metal crossover from the cathode to the anode side could result in the severe capacity fading of the full-cell equipped with the nickel-rich cathodes.[29,124,128,135] During the battery cycling, the dissolved transition metal ions from the cathode side migrated into the anode side and were deposited on the anode.[103,123,125,127,136–137] The deposited transition metal ions promoted the decompositions of the electrolyte solvent during the electrochemical test.[127] The facilitated electrolyte solvent decompositions at the anode side could form unstable anode SEI layer with thick and non-uniform structure, hindering the lithium-ion transport.[52,126] In addition, the extracted transition metal ions provided the vacant site for the migration of the lithium ions into the vacant transition metal sites, therefore, the Li/Ni disordering was facilitated.[9,52] With increasing the upper cut-off voltage (UCV) of the full-cell, the transition metal dissolutions were accelerated due to the enhanced nucleophilic reaction between the cathode and electrolyte. More recently, Gilbert et al. intensively investigated the correlations between the transition metal dissolutions and capacity fading of the full-cell using $LiNi_{0.5}Co_{0.2}Mn_{0.3}O_2$ cathode at different UCV (4.1, 4.2, 4.3, and 4.4 V).[128] As increasing the UCV of the cell, the cells exhibited poor electrochemical performance (Figure 5a). Figure 5b shows the dissolved transition metal concentrations on the cycled graphite anode. Below the UCV of 4.3 V, the manganese ions were the most

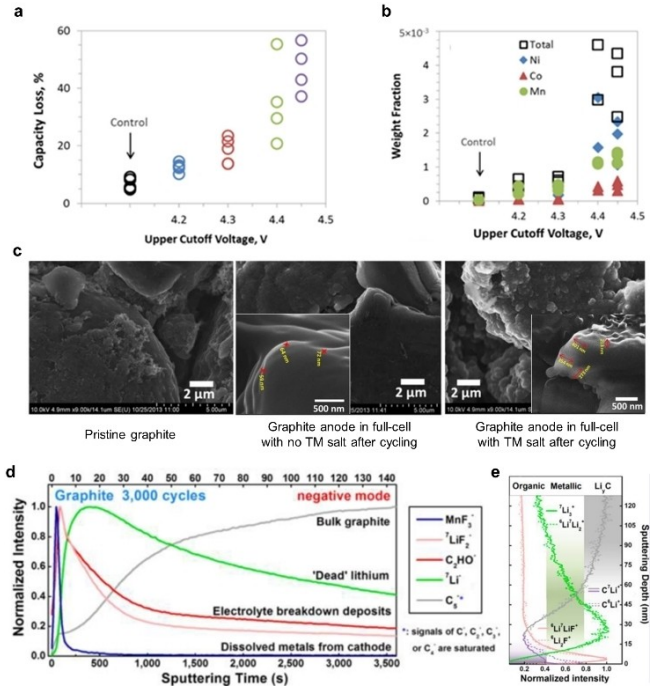


**Figure 5.** Deterioration of anode microstructure: (**a**) Relative discharge capacity loss of the $LiNi_{0.5}Co_{0.2}Mn_{0.3}O_2$/graphite full-cell at the charge cut-off voltage from 4.2 to 4.5 V. (**b**) Relative weight fraction of the dissolved transition metal ions at the graphite anode at charge cut-off voltage from 4.2 to 4.5 V. The control cell was held for 900 h at 3.3 V. Part **a** and **b** were reproduced with permission of Ref. [128]. Copyright 2017, Journal of The Electrochemical Society. (**c**) The scanning electron microscopy (SEM) images of the pristine graphite anode and the cycled graphite after the electrochemical test from the full-cells with and without transition metal salt additives. Reproduced with permission of Ref. [126]. Copyright 2014, The Electrochemical Society. (**d**) ToF-SIMS spectra of the graphite anode after 3,000 cycles at the room temperature. (**e**) Depth profile ToF-SIMS spectra of the graphite anode regarding the lithium containing compounds after 3,000 cycles at the room temperature. Part **d** and **e** were reproduced with permission of Ref. [29]. Copyright 2017, American Chemical Society.

unstable among the three transition metals, which revealed the highest concentrations on the graphite anode. Interestingly, at the UCV $\geq$ 4.4 V, the dissolved transition metal ions found on the anode exhibited similar stoichiometric characteristics (Ni:Co:Mn = 50:20:30) compared with the cathode material ($LiNi_{0.5}Co_{0.2}Mn_{0.3}O_2$). This result implied that the newly exposed primary particles formed by micro-crack evolution were prone to reaction with the acidic species. The enhanced transition metal dissolutions at high UCV contributed to the severe capacity fading of the full-cell, which could be attributed to the irreversible lithium consumption at the anode side.

To better understand the morphological change of the anode SEI layer triggered by dissolved transition metal ions, Fuller et al. evaluated the full cell equipped with the $LiNi_{1/3}Co_{1/3}Mn_{1/3}O_2$ cathode and graphite anode by artificially adding the transition metal (TM) salts as the electrolyte additive.[126] The cycled graphite anode that was evaluated using the TM salts additive showed rough surface morphology; for comparison, the cycled anode with the standard electrolyte retained smooth surface (Figure 5c). Upon close examination of the cycled graphite anodes, the graphite anode with the standard electrolyte exhibited uniform anode SEI layer with the thickness of ~60 nm. By contrast, the thickness of the anode SEI layer was thick and significantly varied from ~200 to ~400 nm in the cycled graphite with the TM salts added in the electrolyte. This result indicated that the TM ions apparently gave rise to the additional solvent decomposition at the anode side, forming thick and non-uniform anode SEI layer. The unstable surface microstructure in the anode contributed to large overpotential and capacity fading during the electrochemical test.[138–140]

More critically, after the long-term cycling, the metallic lithium (dead lithium) was detected on the cycled graphite anode (Figure 5d). The metallic lithium deposition on the anode causes severe capacity and power loss in the full-cell, originating from the irreversible lithium consumption on the graphite anode during the electrochemical cycling.[141] In addition, the formation of the metallic lithium microstructure could give rise to the internal short circuit of the battery.[142] Li et al. demonstrated that evolution of the metallic lithium on the anode originated from the dissolved manganese ions.[29] They revealed that the dissolved manganese ions promote the disruption and additional formation of the anode SEI layer, and the unstable anode SEI layer induced the metallic lithium deposition because of the increased interfacial resistance. As shown in Figure 5e, the lithium elements were distributed as the different compounds such as the SEI layer component (LiF) and metallic lithium at the cycled anode. The organic SEI layer components locally existed at the surface of the graphite-electrolyte interface; for comparison, the metallic lithium was formed underneath the anode SEI layer on extensively cycled anode. Of particular note is that the metallic lithium was formed under normal electrochemical test conditions (at voltage ranged from 3.0 to 4.2 V and room temperature) without any electrochemical strain such as the fast charge and overcharge. Therefore, stabilizing the cathode–electrolyte interface is a key issue for high energy and safe LIBs.

## 3. Strategies to Stabilize the Cathode-Electrolyte Interface

### 3.1. Doping

To mitigate the cathode reactivities with the electrolyte, the surface/bulk doping is the simplest approach among a variety of strategies. Among many candidates for the bulk doping, the incorporation of electrochemically inactive elements into the cathode structure is necessary to ensure the interfacial stability. To date, a wide range of the elements such as the Al,[4,31,143] Ti,[144] Mo,[34] and Nb[36] have been substituted with the nickel ions in the nickel-rich cathode materials. Among such elements, Al is the most appealing element because of their low cost. In case of the Al doping, the $Al^{3+}$ ions were preferentially located at the nickel site compared with the cobalt and manganese site, thereby decreasing the amount of nickel ions at the cathode surface.[31] Furthermore, after the electrochemical test, the $Al^{3+}$ ions in the cathode structure reacted with the acidic

species, which forms nano-sized $LiAlO_2$, $AlF_3$, and $LiAlF_4$ with high ionic conductivity.[31] These ionically conductive compounds did not hinder the lithium-ion transport at the cathode surface, which was fundamentally different to the phosphorus and fluorine containing natural cathode SEI layer. From the structural aspect, the $Al^{3+}$ ions mitigated the lattice oxygen extractions during the delithiation process.[145] The prevented oxygen evolution from the cathode structure suppressed the phase transition from the layered to the rock-salt like structure. Overall, the Al doping into the nickel-rich cathode materials contribute to the structural stability as well as interfacial stability.

Moreover, the introduction of the electrochemically inactive dopants into the bulk lithium site could also contribute to the stable interfacial characteristics in the nickel-rich cathode materials. The Na[35,37] and Mg[32–33] were representative dopants for the substitution of lithium site because the ionic radius of the $Na^+$ and $Mg^{2+}$ ions was similar with the lithium ions. The incorporation of the $Mg^{2+}$ ions into the lithium site reinforced the interatomic bonding strength between transition metal layer and oxygen layer, preventing drastic lattice shrinkage during lithium de-intercalation.[146–147] Furthermore, at the charged state, the $Mg^{2+}$ ions in the lithium site suppressed the structural transformation by inhibiting the spontaneous reduction of the tetravalent nickel ions to the divalent nickel ions.[148] The enhanced structural stability reduced the exothermic reaction with the electrolyte, and the onset temperature about the exothermic reaction shifted towards the higher temperature.[148] Recently, Kim et al. enhanced the structural/interfacial stability of the $LiNiO_2$ cathode by doping the $Na^+$ ions in the lithium site.[37] They demonstrated that the $Na^+$ ions in the cathode structure suppressed the charge disproportionation reactions of the trivalent nickel ions ($2Ni^{3+} \rightarrow Ni^{2+} + Ni^{4+}$), which decreased the Li/Ni disordering. In addition, the $Na^+$ ions that were served as the pillar layer in the lithium site could guarantee the stable interfacial structure because of the restrained spontaneous reduction of the tetravalent nickel ions at fully charge state.

Furthermore, the surface doping approach in the nickel-rich cathode materials could be also effective in stabilizing the cathode–electrolyte interface. Many researchers found that the large amounts of manganese ions at the cathode surface enhanced the structural/thermal stability by mitigating the phase transformation from the layered to the rock-salt like structure.[149–151]

### 3.2. Concentration Gradient

Although the introduction of the electrochemically inactive dopants into the nickel-rich cathodes greatly enhanced the structural/interfacial stability, they were not electrochemically oxidized and reduced during battery cycling, causing the decrease of the energy density. This limitation turns the researchers' highlight into the introduction of the manganese concentration gradient at overall cathode particle while maintaining the cathode compositions. The manganese compositions gradually increased towards the cathode surface; for comparison, the nickel decreased from the core to the surface part. It is noteworthy that the nickel-rich cathodes with the concentration gradient structure exhibited improved structural/chemical stability without reducing reversible capacity by changing the local compositions. The gradual compositional changes in the cathodes gave rise to the morphological changes of the primary particles. The nickel-rich cathodes with the concentration gradient consisted of the radially aligned primary particles towards the core part, which was entirely different with the conventional nickel-rich cathodes with randomly oriented primary particles.[152] More importantly, each aligned primary particle was oriented along the (003) plane, hence facilitating the lithium-ion transport.[153] This high quality layered structure mitigated the micro-crack generation inside the cathode particle because each primary particle exhibited isotropic volume changes during the charging and discharging process.[154–155] With respect to the interfacial stability, the large amount of the electrochemically inactive tetravalent manganese ions at the cathode surface could suppress the manganese ion dissolutions.[152] Furthermore, the lower surface area of the nickel-rich cathodes with concentration gradient than the conventional nickel-rich cathodes could reduce the contact area with the electrolyte, thus improving the chemical stability.[156–157] The morphological integrity also mitigated the cathode reactivities by preventing the penetration of the electrolyte inside the cathode particle. Recently, Sun et al. explicitly demonstrated that the $LiNi_{0.65}Co_{0.13}Mn_{0.22}O_2$ cathode with advanced two-sloped concentration gradient retained stable interface compared with the conventional nickel-rich cathode materials.[156–157] After the storage test at fully charged state of 4.3 V for 4 weeks, the developed $LiNi_{0.65}Co_{0.13}Mn_{0.22}O_2$ cathode showed much lower amount of the dissolved manganese ions (~1 ppm) compared with the $LiNi_{0.65}Co_{0.13}Mn_{0.22}O_2$ without the concentration gradient (~3 ppm). Such stable cathode materials showed the outstanding electrochemical performance in the full-cell configuration with the capacity retention of ~88% after 1,500 cycles.

### 3.3. Porous Structure

The micro-crack evolutions could be delayed through solution based coating method; however, such cracking formation is not completely prevented because of the anisotropic volume changes of each primary particle in the nickel-rich cathode materials with aggregated particle shape. Hence, the morphological collapse during the electrochemical test have remained as inevitable issues in the nickel-rich cathodes. To overcome these issues, many researchers have proposed the porous structured cathode materials to make buffer space for volume changes of the primary particle.[158–160] For example, Kim et al. synthesized the porous structured $LiNi_{0.6}Co_{0.2}Mn_{0.2}O_2$ (NCM) cathode using the polymeric bead clusters during the co-precipitation.[161] In terms of the synthetic procedure, they initially added the polystyrene bead (PSB) as the seed into the co-precipitation reactor, then the transition metals hydroxide

grew on the PSB. During the lithiation process, the PSB was carbonized, inducing the spontaneous reduction of the trivalent nickel ions to the divalent nickel ions. The internal pore in the PSB-NCM caused the accommodation of the generated strain during cycling, leading to morphological and structural integrity. From the interfacial aspect, the intrinsically included inner pore space facilitated the side reactions with the electrolyte, leading to higher film resistance than the conventional nickel-rich cathode at the initial cycle (< 50 cycles). However, as increasing the cycle number, the interfacial resistance was stably maintained in the PSB-NCM; for comparison, the conventional nickel-rich cathode exhibited significant increase of the interfacial resistance because of the severe cracking generations. This result clearly indicated that the morphological robustness in the PSB-NCM during the electrochemical test prevented additional cathode SEI layer formation. The enhanced material integrities allowed outstanding electrochemical performance at the high temperature cycling test compared with the conventional nickel-rich cathodes.

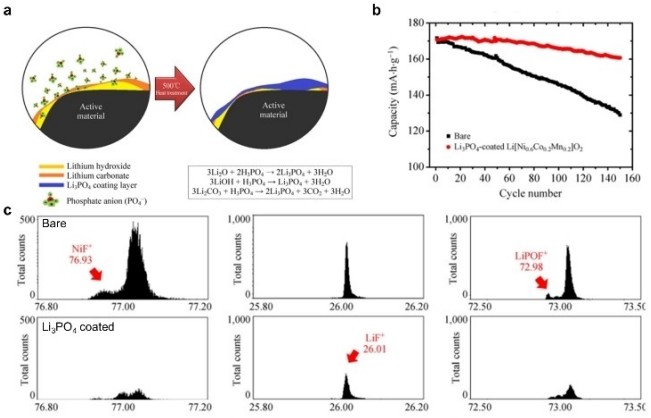


**Figure 6.** Homogeneous surface coating: (**a**) A schematic of the formation mechanism of the $Li_3PO_4$ coating layer. (**b**) Room temperature cycle performance of the bare and $Li_3PO_4$ coated NCM622 in the voltage ranged from 3.0 to 4.3 V. (**c**) ToF-SIMS results of the bare and $Li_3PO_4$ coated NCM622 after 150 cycles at the room temperature. Reproduced with permission of Ref. [122] Copyright 2014, Springer.

### 3.4. Surface coating

The nickel-rich cathode materials with the concentration gradient showed considerable progress in terms of the electrochemical performance. However, the nickel-rich cathodes with the concentration gradient did not retain the surface protective layer, which could deteriorate the interfacial stability of the cathode materials during the electrochemical test. This limitation allowed the researchers to focus on the surface coating such as metal oxide,[46,48,55,133,162–163] metal phosphate,[56,164–165] and lithium reactive coating materials.[40–42,44,51–52,54,122] In terms of the metal oxide, the metal oxide coating materials could mitigate the parasitic redox reaction with the electrolyte.[166] Furthermore, the metal phosphate such as $AlPO_4$,[167] $Ni_3(PO_4)_2$,[168] $Co_3(PO_4)_2$[164] and $MnPO_4$[169] suppressed the surface degradation because of the protection of the cathode materials by the metal phosphate coating layer. Unfortunately, such coating media exhibited ionically and electronically insulating properties, resulting in the increase of the charge transfer resistance.[122] Thus, the critical consideration of the coating material with respect to the conductivity and structural compatibility with the cathode materials were necessary for enhancing the electrochemical performance. For example, the lithium phosphate ($Li_3PO_4$) is a most appealing coating material because it showed high ionic conductivity ($\sim 6\times10^{-8}$ S cm$^{-1}$) and mitigated the cathode reactivities with the electrolyte.[170–171] Jo et al. reported that the introduction of the uniform $Li_3PO_4$ nanolayer with the thickness of < 10 nm into the $LiNi_{0.6}Co_{0.2}Mn_{0.2}O_2$ (NCM622) greatly improved the interfacial stability.[122] As a phosphate source, they utilized the phosphoric acid that could react with the residual lithium compounds such as LiOH and $Li_2CO_3$. The one phosphorus elements could react with three lithium atoms to create the lithium phosphate ($3LiOH$ or $3/2Li_2CO_3 + (PO_4)^{3-} \rightarrow Li_3PO_4$), significantly reducing the residual lithium compounds (Figure 6a). The incorporation of 1 wt.% $Li_3PO_4$ coating layer into the NCM622 substantially decreased the residual lithium compounds with reduced $Li_2CO_3$ content from 3,284 ppm to 738 ppm and LiOH content from 1,736 ppm to 1,197 ppm. The decreased amount of residual lithium compound in combination with the ionically conducting lithium phosphate coating layer contributed to outstanding electrochemical performance. The cycle stability of the $Li_3PO_4$ coated NCM622 was considerably enhanced with the capacity retention of ~94.1% after 150 cycles at room temperature compared with the pristine NCM622 with ~76.1% of original capacity (Figure 6b). Notably, the lithium phosphate nanolayer stably protected the cathode surface against the electrolyte during the electrochemical test (Figure 6c). In terms of the mechanisms for improved interfacial stability, the lithium phosphate adsorbed the moisture in the electrolyte, mitigating the formation of acidic species during the electrochemical cycling. Furthermore, the small amount of the acidic species formed by the $LiPF_6$ salt decompositions easily reacted with the lithium phosphate, forming the $Li_xPO_yF_z$ type compounds. Importantly, the functions of the lithium phosphate about scavenging the moisture and acidic species greatly reduced the transition metal dissolutions from the cathode host structure. In addition, the reduced residual lithium compounds in the $Li_3PO_4$ coated NCM622 suppressed the reactions with the electrolyte, which results in the decreased LiF compounds.

Along with the surface coating layer, it has been reported that the surface protective layer combined with the doping could guarantee the interfacial stability in the nickel-rich cathode materials.[38,40–41,44,51–52] For example, the vanadium-based surface treatment was performed in the $LiNi_{0.8}Co_{0.15}Al_{0.05}O_2$ (NCA) cathodes (Figure 7a).[41] Remarkably, the multi-valent vanadium ions reacted with the residual lithium compounds during the annealing process, ensuring the interfacial stability by mitigating the reactions with the HF. Furthermore, the formation of the electrochemically inactive vanadium oxide such as the $VO_2$ and $V_2O_5$ on the NCA cathode

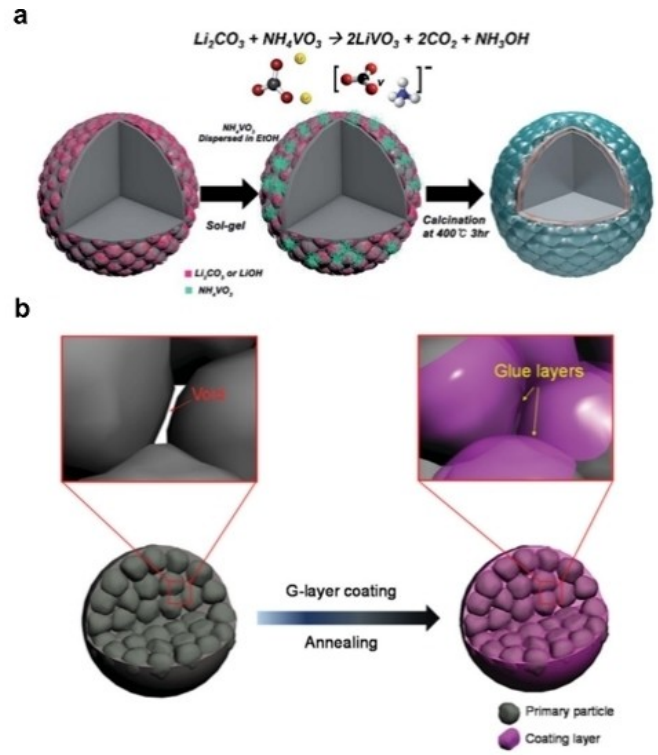


**Figure 7.** Uniform coating layer in combination with the doping: (**a**) A schematic illustration of the formation of the vanadium containing coating layer in the nickel-rich cathode materials with the formation mechanism of the coating layer. Reproduced with permission of Ref. [41]. Copyright 2015, Royal Society of Chemistry. (**b**) A schematic illustrating the formation of the glue layers on the nickel-rich cathode materials. Reproduced with permission of Ref. [44]. Copyright 2016, Wiley

significantly suppressed the side reactions with the electrolyte. Importantly, the tetravalent vanadium ions were doped into the transition metal sites in the cathode structure, creating the vanadium-rich surface layer with the thickness of ~17 nm. Notably, this nanolayer reduced the thickness of cation mixing layer from ~15 nm to ~2 nm, which is responsible for the stable surface structure. Initial thin cation mixing layer was stably maintained even after 200 cycles at 60 °C. This indicated that the spontaneous reduction of the trivalent nickel ions to the divalent nickel ions was highly suppressed, implying that the vanadium coating could assure the interfacial stability.

However, considering that the micro-cracks were continuously evolved in the nickel-rich cathode materials during the charging and discharging process, it is essential to protect newly exposed primary particle to the electrolyte for improving the chemical stability of the cathode. For this purpose, the solution based coating method have been conducted using transition metal containing precursors because the ionized transition metal ions could form coating layer at overall cathode particles. In particular, the cobalt containing structures such as the $LiCoO_2$ and $Li_xCoO_2$ ($0 < x < 1$) as the coating layer could enhance the mechanical strength of the cathode particle by decreasing binding energy between each primary particle (Figure 7b).[40,44] Remarkably, the increased mechanical strength of the cathode particle allowed the morphological integrity even after long-term cycling, thus suppressing the additional formation of the resistant layer inside the cathode.

As discussed earlier, the solution based coating approaches considerably improved the interfacial stability, however, all of the primary particles could not be protected against the electrolyte due to the non-uniform pore distribution in the cathode particle. To effectively stabilize the newly exposed primary particles, Kim et al. incorporated the artificial SEI compounds, which could be electrochemically rearranged, in the $LiNi_{0.84}Co_{0.14}Al_{0.02}O_2$ (NCA) cathode material.[51] In terms of the synthetic process, they mixed the NCA cathode with the cobalt phosphate as the coating precursor, which formed the artificial SEI compounds and transition metal concentration gradient at the surface (Figure 8a). The initial artificial SEI compounds consisting of the phosphorous locally existed with the thickness of ~200 nm only at the surface of the NCA as shown in Figure 8b. Notably, the artificial SEI compounds initially existing on the cathode could be electrochemically rearranged along grain boundaries between each primary particle during battery cycling. This phenomenon was ascribed to the reaction between the artificial SEI compound and the by-products such as acidic species and moisture in the electrolyte. As a result, initial artificial SEI compounds were transformed to the fluorine and hydrogen containing compounds such as $Li_xPF_yO_z$ and $Li_xPF_yH_z$ during the cycling. After only formation cycle, the newly created artificial SEI layer was found inside the cathode particle with the thickness of ~30 nm

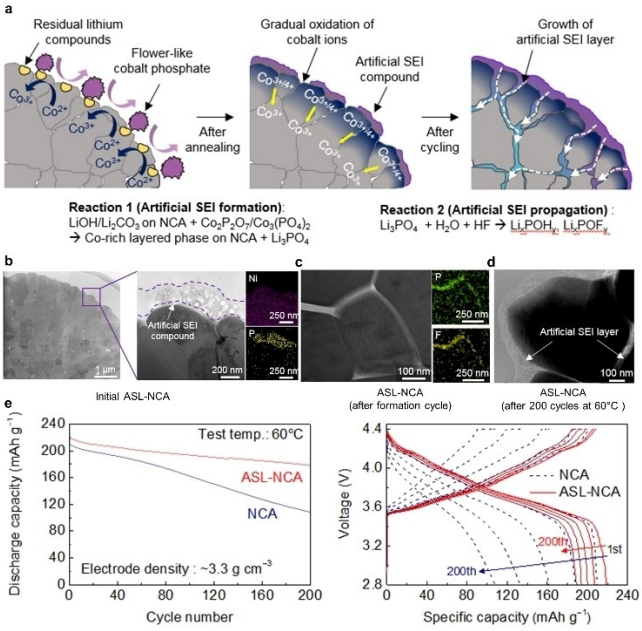


**Figure 8.** Incorporation of the artificial SEI layer: (**a**) A schematic illustration of the formation mechanisms of the artificial SEI compounds with their electrochemical rearrangement phenomenon during the battery cycling. The HAADF-STEM images of (**b**) pristine ASL-NCA and (c) the ASL-NCA after formation cycle with their EDX mapping results. (**d**) A HAADF-STEM image of the ASL-NCA after 200 cycles at 60 °C, indicating that the initial artificial SEI compounds were homogeneously distributed at the cathode particle. (**e**) Cycle performance of the pristine NCA and the ASL-NCA at 60 °C with their voltage profiles at 1, 50, 100, 150, 200 cycles, where the voltage ranged from 2.8 to 4.4 V. Reproduced with permission of Ref. [51]. Copyright 2018, Wiley.

(Figure 8c). Interestingly, the artificial SEI layer was significantly developed after 200 cycles at 60 °C with the increased thickness from ~30 to ~100 nm (Figure 8d). Overall, the electrochemically rearranged artificial SEI layer could protect the newly generated primary particle by micro-crack evolution against the electrolyte. The uniform artificial SEI layer in the artificial SEI layer incorporated NCA (ASL-NCA) allowed the outstanding electrochemical performance at the high temperature of 60 °C. The ASL-NCA retained stable electrochemical performance with the capacity retention of ~81% after 200 cycles compared to the NCA with that of ~51% of original capacity (Figure 8e).

Implantation of advanced surface engineering into the nickel-rich cathode materials have greatly enhanced the structural/interfacial stability of the cathodes. However, in the full-cell equipped with the nickel-rich cathodes, the stable SEI layer on the anode side is a key issue for the development of the high energy full-cell.[29,128,135,172] As discussed earlier, the transition metal crossover from the cathode to the anode side determined the anode microstructure. In particular, the manganese ions mainly affected the anode integrity during the electrochemical cycling.[127–128] Manthiram et al. found that the Al doping into the $LiNi_{0.61}Co_{0.12}Mn_{0.27}O_2$ (NCM) cathode with the concentration gradient contributed to the stable anode microstructure after long-term cycling in the full-cell.[29] The Al doped NCM cathode exhibited the smaller content of dissolved manganese ions than the pristine NCM cathode, mitigating the catalytic electrolyte solvent decompositions at the anode side. The high anode integrity led to outstanding electrochemical performance. The cycle stability of the Al-doped NCM/graphite full-cell was substantially improved with the capacity retention of ~85% after 3,000 cycles compared with the pristine NCA with that of ~65%.

Furthermore, our group recently found that the nickel ion dissolution is an important parameter for achieving stable anode microstructure in the full-cell using the nickel-rich cathodes with nickel contents $\geq$80%.[52] For resolving the nickel-ion crossover issue, the nanoscale epitaxy layer combined with homogeneous transition metal concentration gradient were introduced in the $LiNi_{0.8}Co_{0.1}Mn_{0.1}O_2$ (NCM) cathode.[52] Through the simple dry coating method, the nanostructured stabilizer incorporated NCM (NS-NCM) was synthesized (Figure 9a). With respect to the synthetic process, the cobalt hydroxide as the coating precursor was mixed with the NCM, and the mixtures were annealed at 750 °C. During the annealing process, the cobalt hydroxide was thermally rearranged along grain boundaries between each primary particle because the cobalt hydroxide has low nominal melting temperature of ~168 °C. The uniformly distributed cobalt hydroxide formed the homogeneous transition metal concentration gradient. Moreover, they added much larger amount of the cobalt hydroxide (~4 wt.%) than that of the residual lithium compounds (~1 wt.%). Such non-stoichiometric characteristics between the cobalt and lithium ions led to the formation of surface epitaxy layer (Figure 9b). Notably, the electrochemically inactive $Co_3O_4$ type spinel structure stabilized the cathode structure against the acidic attack, and the $Li_xCoO_2$ ($0<x<1$) type spinel structure contributed to the high electronic

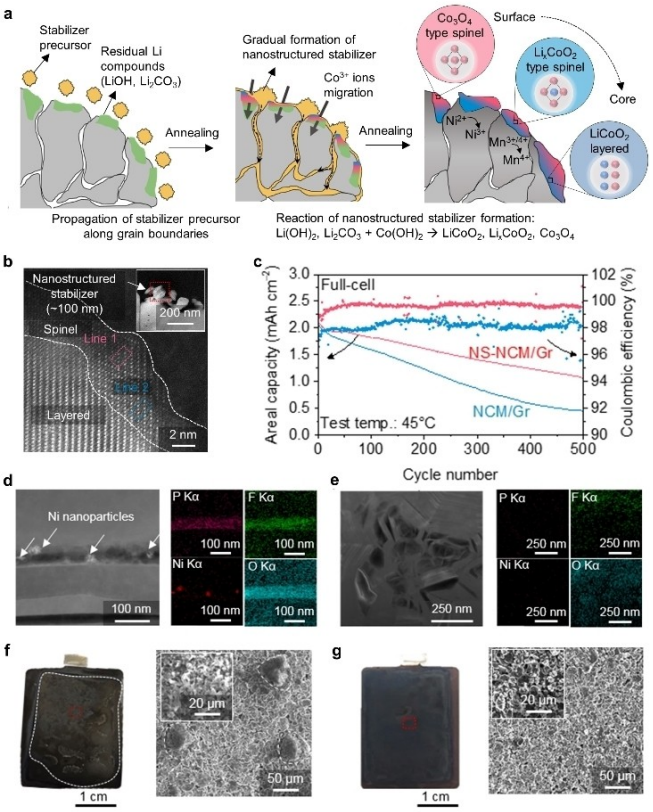


**Figure 9.** A schematic of the synthetic procedure of the NS-NCM, showing that thermally distributed stabilizer precursors formed the surface epitaxy layer and homogeneous transition metal concentration gradients at the overall cathode particle. (**b**) A HAADF-STEM image of the NS-NCM at the red box in the inset image, revealing that the surface coating compound retained the epitaxial structure. (**c**) Full-cell cycle performance at 45 °C, where the voltage ranged from 2.8 to 4.2 V. HAADF-STEM images of the graphite anodes in (**d**) the NCM/graphite full-cell and (**e**) the NS-NCM/graphite full-cell after 500 cycles at 45 °C with their EDX mapping results. Photograph images of the graphite anode in (**f**) the NCM/graphite full-cell and (**g**) the NS-NCM/graphite anode after 500 cycles at 45 °C with their SEM images at the marked red box. Reproduced with permission of Ref. [52]. Copyright 2018, Royal Society of Chemistry.

conductivity. In addition, the homogeneous transition metal concentration gradient at overall cathode particle gave rise to the oxidation of the divalent nickel ions to the trivalent nickel ions, which contributed to the mitigated nickel ions dissolutions. These characteristics significantly enhanced the electrochemical performance of the NS-NCM in the full-cell configuration. The NS-NCM/graphite full-cell retained much better cycling performance than the NCM/graphite full-cell at 45 °C as presented in Figure 9c. Interestingly, the bright metallic nickel particles were observed the cycled graphite anode in the NCM/graphite full-cell, contributing to additional anode SEI layer formation (Figure 9d). By contrast, inside the cycled graphite anode in the NS-NCM/graphite full-cell, the formation of the anode SEI layer was significantly mitigated, which was ascribed to the restrained nickel ion crossover from the cathode side (Figure 9e). More seriously, the unstable anode SEI layer in the NCM/graphite full-cell caused the metallic lithium depositions at the surface of the graphite anode because of the increased

interfacial resistance. As shown in Figure 9f, the massive metallic lithium with the size of ~50 μm formed on overall graphite anode. On the contrary, the cycled graphite anode in the NS-NCM/graphite full-cell revealed the clean surface without any trace of the metallic lithium, indicating that the nickel ion crossovers mainly affected the anode integrity (Figure 9g).

### 3.5. Crystallinity Tuning

The intrinsic properties of the polycrystalline nickel-rich cathode materials is that the cathode particles underwent the micro-crack evolutions during the battery cycle test.[67] Although above mentioned approaches could mitigate the reactivity of the cathode particles with the electrolyte, the newly created surface by the micro-cracks in the polycrystalline cathode particle could eventually cause the interfacial instability after the long-term cycling test. In this regard, many researchers have proposed the single crystalline nickel-rich cathodes to completely prevent the micro-crack evolutions.[57–66] For the polycrystalline nickel-rich cathode materials, the anisotropic volume changes of each primary particle caused the micro-crack evolution during the continuous charging and discharging process (Figure 10a).[14–15] The collapsed particle increases the contact area with the electrolyte, giving rise to the formation of resistant layer such as the cation mixing layer and cathode SEI layer.[16] After long-term cycling, the continuous micro-crack generations hinder the lithium-ion transport, leading to severe capacity fading. By contrast, the single crystalline nickel-rich cathodes do not exhibit the cracking formation because of the isotropic volume change during the electrochemical test (Figure 10b).[67] This indicates that the original morphology could be stably maintained even after the long-term cycling. Of particular note is that the morphological integrity could suppress continuous formation of the resistant layer during the electrochemical test, allowing outstanding electrochemical performance.

Recently, Xiong et al. compared the oxygen release between polycrystalline and single crystalline $LiNi_{0.5}Mn_{0.3}Co_{0.2}O_2$ (NMC532) cathode through thermogravimetric analysis coupled with mass spectrometry (TGA-MS).[64] The phase transition from the layered to the rock-salt like structure generated oxygen species, which induces the oxidative decomposition (pseudo-combustion) of the electrolyte and cathode SEI layer.[100–102] Such structural and interfacial instabilities have been known as the main capacity fading mechanisms of the nickel-rich cathode materials. To measure the released oxygen gas from the cathode materials, all cells were charged at 4.6 V, and the temperature of the cells increased to 350 °C (Figure 10c). The polycrystalline NMC532 cathode (uncoated, $Al_2CO_3$ coated, and HV coated sample) revealed the lower onset temperature which the oxygen gas stated to be evolved than the single crystalline NMC532 cathode materials. In addition, to further investigate the stability of the cathode materials at the high voltage, the all cells were charged at 4.6 V and held for 420 h (Figure 10d). As expected from the thermal aggravation test, the single crystalline NCM523 evolved the least oxygen gas among all samples. These results clearly suggest that the lack of grain boundaries in the single crystalline cathodes could limit oxygen release, assuring the battery safety even at the high voltage.

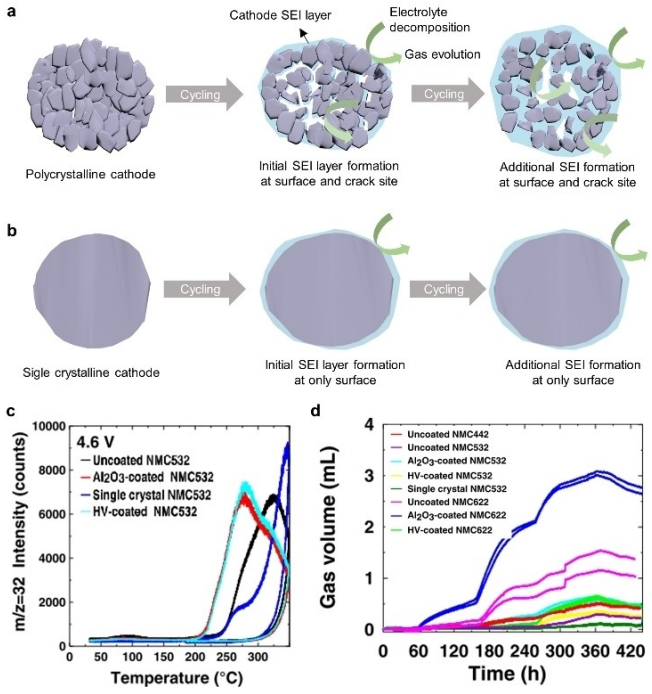


**Figure 10.** Single crystalline nickel-rich cathode materials: Schematics of morphological and interfacial changes of (**a**) the polycrystalline cathode and (**b**) the single crystalline cathode during the electrochemical test. Part **a** and **b** were reproduced with permission of Ref. [67]. Copyright 2018, Wiley. (**c**) Mass spectroscopy result ($m/z = 32$) of the polycrystalline cathode (Uncoated NMC532, $Al_2O_3$ coated NMC532, HV-coated NMC532) and the single crystalline NMC532 at the fully charged state (4.6 V) as the function of temperature. (**d**) Volume changes of the produced gas of different NMC532 and NMC622 samples when the cells were charged and held at different voltage (4.4, 4.5, and 4.6 V). Part c and d were reproduced with permission of Ref. [64]. Copyright 2017, The Electrochemical Society.

## 4. Summary and Outlook

In this review, we have summarized the dynamic behavior of the nickel-rich NCM cathode-electrolyte interface and a variety of strategies to mitigate the cathode reactivity with the electrolyte. The spontaneous reduction of the transition metal ions in the cathode structure have a crucial role in determining the interfacial stability, which was attributed to the oxidative electrolyte solvent decompositions. When the cathodes were only exposed to the electrolyte without the electrical bias, the thin cathode SEI layer was formed. During the battery cycling, this thin SEI layer was significantly developed, impeding the lithium-ion transport. With respect to the structural aspect, the reduction of the nickel ions facilitated the irreversible phase transformation at the cathode surface. Furthermore, the acidic species that were formed by the decompositions of the $LiPF_6$ salt and PVdF binder could dissolve the transition metal ions from the cathode side, which passivates both the cathode and conducting agent. More seriously, the extracted transition

metal ions were redeposited in the anode side, where the formation of anode SEI layer was promoted by the enhanced electrolyte decomposition reactions. In addition, the increased interfacial resistance by the unstable anode SEI layer could cause the metallic lithium depositions throughout the anode, strongly threatening the battery safety.

Along with the unstable electrochemical properties of the nickel ions, the nickel-rich cathodes with the morphology of secondary particle exhibited severe cracking formation inside the cathode particles after prolonged cycling. Such morphological collapse increases the chemical reactivity of the cathode materials with the electrolyte, accelerating the formation of the resistant layer inside the cathode particles. To date, the incorporation of the surface coating layer and concentration gradient into the nickel-rich cathode materials greatly improved the interfacial stability. However, the continuous microcrack generation during the electrochemical test could not completely ensure the stable interfacial structure between the cathode and electrolyte. This limitation regarding the polycrystalline nickel-rich cathodes encourage the researchers to focus on the single crystalline cathodes. The lack of grain boundaries in the single crystalline cathodes could guarantee the long-term cycling stability and safety issue because the cathodes maintained the original morphology even after long-term cycling. Finally, on the basis of this review, we believe that the single crystalline cathode combined with the surface coating and doping approaches is a most appealing material, and opens a new avenue for high energy LIBs.

## Acknowledgements

*This work was supported by the Korea Institute of Energy Technology Evaluation and Planning (KETEP) and the Ministry of Trade, Industry & Energy(MOTIE) of the Republic of Korea (No. 20172410100140). Also, Finical support from the 2020 Research Funds (1.200029.1) of Ulsan National Institute of Science and Technology (UNIST) was greatly acknowledged. Furthermore. P. Oh acknowledged the Pukyong National University Research Fund in 2018 (CD20180568).*

## Conflict of Interest

The authors declare no conflict of interest.

**Keywords:** nickel-rich cathodes · interfacial stability · solid-electrolyte interphase · electrolyte decompositions · single crystalline characteristics

[1] M. Armand, J. M. Tarascon, *Nature.* **2008**, *451*, 652–657.
[2] N.-S. Choi, Z. Chen, S. A. Freunberger, X. Ji, Y.-K. Sun, K. Amine, G. Yushin, L. F. Nazar, J. Cho, P. G. Bruce, *Angew. Chem. Int. Ed.* **2012**, *51*, 9994–10024; *Angew. Chem.* **2012**, *124*, 10134–10166.
[3] T.-H. Kim, J.-S. Park, S. K. Chang, S. Choi, J. H. Ryu, H.-K. Song, *Adv. Energy Mater.* **2012**, *2*, 860–872.
[4] T. Ohzuku, A. Ueda, M. Kouguchi, *J. Electrochem. Soc.* **1995**, *142*, 4033–4039.
[5] H. Arai, S. Okada, Y. Sakurai, J.-i. Yamaki, *Solid State Ionics.* **1998**, *109*, 295–302.
[6] Y.-K. Sun, S.-T. Myung, B.-C. Park, J. Prakash, I. Belharouak, K. Amine, *Nat. Mater.* **2009**, *8*, 320–324.
[7] B. Scrosati, J. Garche, *J. Power Sources.* **2010**, *195*, 2419–2430.
[8] P. Oh, M. Ko, S. Myeong, Y. Kim, J. Cho, *Adv. Energy Mater.* **2014**, *4*.
[9] W. Liu, P. Oh, X. Liu, M.-J. Lee, W. Cho, S. Chae, Y. Kim, J. Cho, *Angew. Chem. Int. Ed.* **2015**, *54*, 4440–4457; *Angew. Chem.* **2015**, *127*, 4518–4536.
[10] M. Gu, I. Belharouak, J. Zheng, H. Wu, J. Xiao, A. Genc, K. Amine, S. Thevuthasan, D. R. Baer, J. G. Zhang, N. D. Browning, J. Liu, C. Wang, *ACS Nano.* **2013**, *7*, 760–767.
[11] K. Dokko, M. Nishizawa, S. Horikoshi, T. Itoh, M. Mohamedi, I. Uchida, *Electrochem. Solid-State Lett.* **2000**, *3*, 125–127.
[12] S. K. Jung, H. Gwon, J. Hong, K. Y. Park, D. H. Seo, H. Kim, J. Hyun, W. Yang, K. Kang, *Adv. Energy Mater.* **2014**, *4*, 1300787.
[13] F. Lin, I. M. Markus, D. Nordlund, T. C. Weng, M. D. Asta, H. L. Xin, M. M. Doeff, *Nat. Commun.* **2014**, *5*, 3529–3537.
[14] K. Dokko, *Electrochem. Solid-State Lett.* **1999**, *3*, 125–127.
[15] A. Mukhopadhyay, B. W. Sheldon, *Prog. Mater. Sci.* **2014**, *63*, 58–116.
[16] S. Watanabe, M. Kinoshita, T. Hosokawa, K. Morigaki, K. Nakura, *J. Power Sources.* **2014**, *258*, 210–217.
[17] K. Xu, *Chem. Rev.* **2014**, *114*, 11503–11618.
[18] M. Gauthier, T. J. Carney, A. Grimaud, L. Giordano, N. Pour, H.-H. Chang, D. P. Fenning, S. F. Lux, O. Paschos, C. Bauer, F. Maglia, S. Lupart, P. Lamp, Y. Shao-Horn, *J. Phys. Chem. Lett.* **2015**, *6*, 4653–4672.
[19] D. Takamatsu, Y. Koyama, Y. Orikasa, S. Mori, T. Nakatsutsumi, T. Hirano, H. Tanida, H. Arai, Y. Uchimoto, Z. Ogumi, *Angew. Chem. Int. Ed.* **2012**, *51*, 11597–11601; *Angew. Chem.* **2012**, *124*, 11765–11769.
[20] K. Yamamoto, T. Minato, S. Mori, D. Takamatsu, Y. Orikasa, H. Tanida, K. Nakanishi, H. Murayama, T. Masese, T. Mori, H. Arai, Y. Koyama, Z. Ogumi, Y. Uchimoto, *J. Phys. Chem. C* **2014**, *118*, 9538–9543.
[21] D. Aurbach, A. Zaban, A. Schechter, Y. Ein-Eli, E. Zinigrad, B. Markovsky, *J. Electrochem. Soc.* **1995**, *142*, 2873–2882.
[22] D. Aurbach, I. Weissman, A. Schechter, H. Cohen, *Langmuir.* **1996**, *12*, 3991–4007.
[23] K. Kanamura, S. Toriyama, S. Shiraishi, M. Ohashi, Z.-I. Takehara, *J. Electroanal. Chem.* **1996**, *419*, 77–84.
[24] D. H. Jang, Y. J. Shin, S. M. Oh, *J. Electrochem. Soc.* **1996**, *143*, 2204–2211.
[25] D. Aurbach, B. Markovsky, A. Rodkin, E. Levi, Y. S. Cohen, H. J. Kim, M. Schmidt, *Electrochim. Acta.* **2002**, *47*, 4291–4306.
[26] E. Markevich, G. Salitra, D. Aurbach, *Electrochem. Commun.* **2005**, *7*, 1298–1304.
[27] I. H. Cho, S.-S. Kim, S. C. Shin, N.-S. Choi, *Electrochem. Solid-State Lett.* **2010**, *13*, A168–A172.
[28] W. Li, A. Dolocan, P. Oh, H. Celio, S. Park, J. Cho, A. Manthiram, *Nat. Commun.* **2017**, *8*, 14589.
[29] W. Li, U. H. Kim, A. Dolocan, Y. K. Sun, A. Manthiram, *ACS Nano.* **2017**, *11*, 5853–5863.
[30] H. Liu, J. Li, Z. Zhang, Z. Gong, Y. Yang, *Electrochim. Acta.* **2004**, *49*, 1151–1159.
[31] D. Aurbach, O. Srur-Lavi, C. Ghanty, M. Dixit, O. Haik, M. Talianker, Y. Grinblat, N. Leifer, R. Lavi, D. T. Major, G. Goobes, E. Zinigrad, E. M. Erickson, M. Kosa, B. Markovsky, J. Lampert, A. Volkov, J.-Y. Shin, A. Garsuch, *J. Electrochem. Soc.* **2015**, *162*, A1014–A1027.
[32] Z. Huang, Z. Wang, X. Zheng, H. Guo, X. Li, Q. Jing, Z. Yang, *Electrochim. Acta.* **2015**, *182*, 795–802.
[33] Z. Huang, Z. Wang, H. Guo, X. Li, *J. Alloys Compd.* **2016**, *671*, 479–485.
[34] Y. Li, Q. Su, Q. Han, P. Li, L. Li, C. Xu, X. Cao, G. Cao, *Ceram. Int.* **2017**, *43*, 3483–3488.
[35] D.-L. Vu, J.-w. Lee, *J. Solid State Electrochem.* **2017**.
[36] Z. Yang, W. Xiang, Z. Wu, F. He, J. Zhang, Y. Xiao, B. Zhong, X. Guo, *Ceram. Int.* **2017**, *43*, 3866–3872.
[37] H. Kim, A. Choi, S. W. Doo, J. Lim, Y. Kim, K. T. Lee, *J. Electrochem. Soc.* **2018**, *165*, A201–A205.
[38] Y. Cho, P. Oh, J. Cho, *Nano Lett.* **2013**, *13*, 1145–1152.
[39] Y. P. Chen, Y. Zhang, B. J. Chen, Z. Y. Wang, C. Lu, *J. Power Sources.* **2014**, *256*, 20–27.
[40] H. Kim, M. G. Kim, H. Y. Jeong, H. Nam, J. Cho, *Nano Lett.* **2015**, *15*, 2111–2119.
[41] M. J. Lee, M. Noh, M. H. Park, M. Jo, H. Kim, H. Nam, J. Cho, *J. Mater. Chem. A* **2015**, *3*, 13453–13460.

[42] I. H. Son, J. H. Park, S. Kwon, J. Mun, J. W. Choi, *Chem. Mater.* **2015**, *27*, 7370–7379.
[43] J. Yang, Y. Xia, *ACS Appl. Mater. Interfaces.* **2016**. 8, 1297–1308.
[44] H. Kim, S. Lee, H. Cho, J. Kim, J. Lee, S. Park, S. H. Joo, S. H. Kim, Y. G. Cho, H. K. Song, S. K. Kwak, J. Cho, *Adv. Mater.* **2016**, *28*, 4705–4712.
[45] S. Liu, H. Wu, L. Huang, M. Xiang, H. Liu, Y. Zhang, *J. Alloys Compd.* **2016**, *674*, 447–454.
[46] Y. Huang, Y. Huang, X. Hu, *Electrochim. Acta* **2017**, *231*, 294–299.
[47] Y. Li, H. Yu, Y. Hu, H. Jiang, C. Li, *J. Energy Chem.* **2018**. *27*, 559–564.
[48] B.-S. Liu, X.-L. Sui, S.-H. Zhang, F.-D. Yu, Y. Xue, Y. Zhang, Y.-X. Zhou, Z.-B. Wang, *J. Alloys Compd.* **2017**.
[49] M. Wang, R. Zhang, Y. Gong, Y. Su, D. Xiang, L. Chen, Y. Chen, M. Luo, M. Chu, *Solid State Ionics.* **2017**, *312*, 53–60.
[50] S. Zhou, G. Wang, W. Tang, Y. Xiao, K. Yan, *Electrochim. Acta.* **2018**. *261*, 565–577.
[51] J. Kim, J. Lee, H. Ma, H. Y. Jeong, H. Cha, H. Lee, Y. Yoo, M. Park, J. Cho, *Adv. Mater.* **2018**, *30*, 1704309.
[52] J. Kim, H. Ma, H. Cha, H. Lee, J. Sung, M. Seo, P. Oh, M. Park, J. Cho, *Energy Environ. Sci.* **2018**, *11*, 1449–1459.
[53] W. Liu, X. Li, D. Xiong, Y. Hao, J. Li, H. Kou, B. Yan, D. Li, S. Lu, A. Koo, K. Adair, X. Sun, *Nano Energy.* **2018**, *44*, 111–120.
[54] K. Min, K. Park, S. Y. Park, S.-W. Seo, B. Choi, E. Cho, *J. Electrochem. Soc.* **2018**, *165*, A79–A85.
[55] F. Schipper, H. Bouzaglo, M. Dixit, E. M. Erickson, T. Weigel, M. Talianker, J. Grinblat, L. Burstein, M. Schmidt, J. Lampert, C. Erk, B. Markovsky, D. T. Major, D. Aurbach, *Adv. Energy Mater.* **2018**, *8*, 1701682.
[56] C. Yao, Y. Mo, X. Jia, X. Chen, J. Xia, Y. Chen, *Solid State Ionics.* **2018**, *317*, 156–163.
[57] Y. Kim, *ACS Appl. Mater. Interfaces.* **2012**, *4*, 2329–2333.
[58] T. Kimijima, N. Zettsu, K. Yubuta, K. Hirata, K. Kami, K. Teshima, *J. Mater. Chem. A.* **2016**, *4*, 7289–7296.
[59] L. Wang, B. Wu, D. Mu, X. Liu, Y. Peng, H. Xu, Q. Liu, L. Gai, F. Wu, *J. Alloys Compd.* **2016**, *674*, 360–367.
[60] X. Jiang, S. Chu, Y. Chen, Y. Zhong, Y. Liu, Z. Shao, *J. Alloys Compd.* **2017**, *691*, 206–214.
[61] J. Li, A. R. Cameron, H. Li, S. Glazier, D. Xiong, M. Chatzidakis, J. Allen, G. A. Botton, J. R. Dahn, *J. Electrochem. Soc.* **2017**, *164*, A1534–A1544.
[62] J. Li, H. Li, W. Stone, R. Weber, S. Hy, J. R. Dahn, *J. Electrochem. Soc.* **2017**, *164*, A3529–A3537.
[63] R. Weber, C. R. Fell, J. R. Dahn, S. Hy, *J. Electrochem. Soc.* **2017**, *164*, A2992–A2999.
[64] D. J. Xiong, L. D. Ellis, J. Li, H. Li, T. Hynes, J. P. Allen, J. Xia, D. S. Hall, I. G. Hill, J. R. Dahn, *J. Electrochem. Soc.* **2017**, *164*, A3025–A3037.
[65] H. Li, J. Li, X. Ma, J. R. Dahn, *J. Electrochem. Soc.* **2018**, *165*, A1038–A1045.
[66] J. Li, H. Li, W. Stone, S. Glazier, J. R. Dahn, *J. Electrochem. Soc.* **2018**, *165*, A626–A635.
[67] J. Kim, H. Lee, H. Cha, M. Yoon, M. Park, J. Cho, *Adv. Energy Mater.* **2018**, *8*, 1702028.
[68] C. Cao, J. Zhang, X. Xie, B. Xia, *Ionics.* **2017**, *23*, 1337–1356.
[69] Z. Chen, D. Chao, J. Lin, Z. Shen, *Mater. Res. Bull.* **2017**, *96*, 491–502.
[70] Y. Ding, D. Mu, B. Wu, R. Wang, Z. Zhao, F. Wu, *Appl. Energy.* **2017**, *195*, 586–599.
[71] Y. Ding, R. Wang, L. Wang, K. Cheng, Z. Zhao, D. Mu, B. Wu, *Energy Procedia.* **2017**, *105*, 2941–2952.
[72] A. Konarov, S.-T. Myung, Y.-K. Sun, *ACS Energy Lett.* **2017**, 703–708.
[73] W. Liu, P. Oh, X. Liu, M.-J. Lee, W. Cho, S. Chae, Y. Kim, J. Cho, *Angew. Chem. Int. Ed.* **2015**, *54*, 4440–4457; *Angew. Chem.* **2015**, *127*, 4518–4536.
[74] A. Manthiram, J. C. Knight, S.-T. Myung, S.-M. Oh, Y.-K. Sun, *Adv. Energy Mater.* **2016**, *6*, n/a-n/a.
[75] A. Manthiram, B. Song, W. Li, *Energy Storage Mater.* **2017**, *6*, 125–139.
[76] S.-T. Myung, F. Maglia, K.-J. Park, C. S. Yoon, P. Lamp, S.-J. Kim, Y.-K. Sun, *ACS Energy Lett.* **2016**, *196–223*.
[77] F. Schipper, D. Aurbach, *Russ. J. Electrochem.* **2016**, *52*, 1095–1121.
[78] F. Schipper, E. M. Erickson, C. Erk, J. Y. Shin, F. F. Chesneau, D. Aurbach, *J. Electrochem. Soc.* **2017**, *164*, A6220–A6228.
[79] C. Tian, F. Lin, M. M. Doeff, *Acc. Chem. Res.* **2018**, *51*, 89–96.
[80] H. Zhang, H. Zhao, M. A. Khan, W. Zou, J. Xu, L. Zhang, J. Zhang, *J. Mater. Chem. A.* **2018**, *6*, 20564–20620.
[81] J. B. Goodenough, Y. Kim, *Chem. Mater.* **2010**, *22*, 587–603.
[82] J. B. Goodenough, *Acc. Chem. Res.* **2013**, *46*, 1053–1061.
[83] Y. Wang, S. Nakamura, M. Ue, P. B. Balbuena, *J. Am. Chem. Soc.* **2001**, *123*, 11708–11718.
[84] X. Zhang, J. K. Pugh, P. N. Ross, *J. Electrochem. Soc.* **2001**, *148*, E183–E188.
[85] J. M. Vollmer, L. A. Curtiss, D. R. Vissers, K. Amine, *J. Electrochem. Soc.* **2004**, *151*, A178–A183.
[86] O. Borodin, T. R. Jow, *ECS Trans.* **2011**, *33*, 77–84.
[87] L. Xing, O. Borodin, G. D. Smith, W. Li, *J. Phys. Chem. A.* **2011**, *115*, 13896–13905.
[88] K. Leung, *J. Phys. Chem. C.* **2013**, *117*, 1539–1547.
[89] L. Johnson, C. Li, Z. Liu, Y. Chen, S. A. Freunberger, P. C. Ashok, B. B. Praveen, K. Dholakia, J.-M. Tarascon, P. G. Bruce, *Nat. Chem.* **2014**, *6*, 1091.
[90] M. K. Rahman, Y. Saito, *J. Power Sources.* **2007**, *174*, 889–894.
[91] G. Cherkashinin, K. Nikolowski, H. Ehrenberg, S. Jacke, L. Dimesso, W. Jaegermann, *Phys. Chem. Chem. Phys.* **2012**, *14*, 12321–12331.
[92] G. Cherkashinin, M. Motzko, N. Schulz, T. Späth, W. Jaegermann, *Chem. Mater.* **2015**, *27*, 2875–2887.
[93] S. Zheng, R. Huang, Y. Makimura, Y. Ukyo, C. A. J. Fisher, T. Hirayama, Y. Ikuhara, *J. Electrochem. Soc.* **2011**, *158*, A357–A362.
[94] D. P. Abraham, R. D. Twesten, M. Balasubramanian, I. Petrov, J. McBreen, K. Amine, *Electrochem. Commun.* **2002**, *4*, 620–625.
[95] S. M. Bak, K. W. Nam, W. Chang, X. Yu, E. Hu, S. Hwang, E. A. Stach, K. B. Kim, K. Y. Chung, X. Q. Yang, *Chem. Mater.* **2013**, *25*, 337–351.
[96] S. Venkatraman, Y. Shin, A. Manthiram, *Electrochem. Solid-State Lett.* **2003**, *6*, A9–A12.
[97] K. Kumai, K. Takei, Y. Kobayashi, H. Miyashiro, R. Ishikawa, *Electrochemistry.* **1998**, *66*, 314–320.
[98] R. Imhof, P. Novák, *J. Electrochem. Soc.* **1999**, *146*, 1702–1706.
[99] K. Kumai, H. Miyashiro, Y. Kobayashi, K. Takei, R. Ishikawa, *J. Power Sources.* **1999**, *81–82*, 715–719.
[100] I. Belharouak, W. Lu, D. Vissers, K. Amine, *Electrochem. Commun.* **2006**, *8*, 329–335.
[101] I. Belharouak, D. Vissers, K. Amine, *J. Electrochem. Soc.* **2006**, *153*, A2030–A2035.
[102] Y. Wang, J. Jiang, J. R. Dahn, *Electrochem. Commun.* **2007**, *9*, 2534–2540.
[103] J. Vetter, P. Novák, M. R. Wagner, C. Veit, K. C. Möller, J. O. Besenhard, M. Winter, M. Wohlfahrt-Mehrens, C. Vogler, A. Hammouche, *J. Power Sources.* **2005**, *147*, 269–281.
[104] D. Aurbach, M. D. Levi, E. Levi, H. Teller, B. Markovsky, G. Salitra, U. Heider, L. Heider, *J. Electrochem. Soc.* **1998**, *145*, 3024–3034.
[105] M. Shikano, H. Kobayashi, S. Koike, H. Sakaebe, E. Ikenaga, K. Kobayashi, K. Tatsumi, *J. Power Sources.* **2007**, *174*, 795–799.
[106] D. Aurbach, *J. Power Sources.* **2000**, *89*, 206–218.
[107] M. Onuki, S. Kinoshita, Y. Sakata, M. Yanagidate, Y. Otake, M. Ue, M. Deguchi, *J. Electrochem. Soc.* **2008**, *155*, A794–A797.
[108] L. Xing, W. Li, C. Wang, F. Gu, M. Xu, C. Tan, J. Yi, *J. Phys. Chem. B* **2009**, *113*, 16596–16602.
[109] L. Xing, O. Borodin, *Phys. Chem. Chem. Phys.* **2012**, *14*, 12838–12843.
[110] R. Robert, C. Bunzli, E. J. Berg, P. Novak, *Chem. Mater.* **2015**, *27*, 526–536.
[111] B. B. Berkes, A. Schiele, H. Sommer, T. Brezesinski, J. Janek, *J. Solid State Electrochem.* **2016**, *20*, 2961–2967.
[112] Z. W. Lebens-Higgins, S. Sallis, N. V. Faenza, F. Badway, N. Pereira, D. M. Halat, M. Wahila, C. Schlueter, T. L. Lee, W. L. Yang, C. P. Grey, G. G. Amatucci, L. F. J. Piper, *Chem. Mater.* **2018**, *30*, 958–969.
[113] S. E. Sloop, J. K. Pugh, S. Wang, J. B. Kerr, K. Kinoshita, *Electrochem. Solid-State Lett.* **2001**, *4*, A42–A44.
[114] S.-T. Myung, K. Amine, Y.-K. Sun, *J. Mater. Chem.* **2010**, *20*, 7074–7095.
[115] K. Tasaki, A. Goldberg, J. J. Lian, M. Walker, A. Timmons, S. J. Harris, *J. Electrochem. Soc.* **2009**, *156*, A1019–A1027.
[116] Y. S. Jung, P. Lu, A. S. Cavanagh, C. Ban, G. H. Kim, S. H. Lee, S. M. George, S. J. Harris, A. C. Dillon, *Adv. Energy Mater.* **2013**, *3*, 213–219.
[117] A. Grenier, H. Liu, K. M. Wiaderek, Z. W. Lebens-Higgins, O. J. Borkiewicz, L. F. J. Piper, P. J. Chupas, K. W. Chapman, *Chem. Mater.* **2017**, *29*, 7345–7352.
[118] A. M. Andersson, D. P. Abraham, R. Haasch, S. MacLaren, J. Liu, K. Amine, *J. Electrochem. Soc.* **2002**, *149*, A1358–A1369.
[119] D. H. Cho, C. H. Jo, W. Cho, Y. J. Kim, H. Yashiro, Y. K. Sun, S. T. Myung, *J. Electrochem. Soc.* **2014**, *161*, A920–A926.
[120] S. Watanabe, T. Hosokawa, K. I. Morigaki, M. Kinoshita, K. Nakura, *ECS Trans.* **2012**, *41*, 65–74.
[121] H.-H. Chang, C.-C. Chang, C.-Y. Su, H.-C. Wu, M.-H. Yang, N.-L. Wu, *J. Power Sources.* **2008**, *185*, 466–472.
[122] C. H. Jo, D. H. Cho, H. J. Noh, H. Yashiro, Y. K. Sun, S. T. Myung, *Nano Res.* **2014**.

[123] D. P. Abraham, T. Spila, M. M. Furczon, E. Sammann, *Electrochem. Solid-State Lett.* **2008**, *11*, A226–A228.
[124] I. H. Cho, S.-S. Kim, S. C. Shin, N.-S. Choi, *Electrochem. Solid-State Lett.* **2010**, *13*, A168–A172.
[125] C. Delacourt, A. Kwong, X. Liu, R. Qiao, W. L. Yang, P. Lu, S. J. Harris, V. Srinivasan, *J. Electrochem. Soc.* **2013**, *160*, A1099–A1107.
[126] T. Joshi, K. Eom, G. Yushin, T. F. Fuller, *J. Electrochem. Soc.* **2014**, *161*, A1915–A1921.
[127] X. Xiao, Z. Liu, L. Baggetto, G. M. Veith, K. L. More, R. R. Unocic, *Phys. Chem. Chem. Phys.* **2014**, *16*, 10398–10402.
[128] J. A. Gilbert, I. A. Shkrob, D. P. Abraham, *J. Electrochem. Soc.* **2017**, *164*, A389–A399.
[129] R. J. Gummow, A. de Kock, M. M. Thackeray, *Solid State Ionics.* **1994**, *69*, 59–67.
[130] Y. Xia, Y. Zhou, M. Yoshio, *J. Electrochem. Soc.* **1997**, *144*, 2593–2600.
[131] A. Du Pasquier, A. Blyr, P. Courjal, D. Larcher, G. Amatucci, B. Gérand, J. M. Tarascon, *J. Electrochem. Soc.* **1999**, *146*, 428–436.
[132] J.-S. Kim, K. Kim, W. Cho, W. H. Shin, R. Kanno, J. W. Choi, *Nano Lett.* **2012**, *12*, 6358–6365.
[133] S.-T. Myung, K. Izumi, S. Komaba, Y.-K. Sun, H. Yashiro, N. Kumagai, *Chem. Mater.* **2005**, *17*, 3695–3704.
[134] A. Manthiram, J. C. Knight, S. T. Myung, S. M. Oh, Y. K. Sun, *Adv. Energy Mater.* **2016**, *6*, 1501010-n/a.
[135] H. Tsunekawa, a. Tanimoto, Satoshi, R. Marubayashi, M. Fujita, K. Kifune, M. Sano, *J. Electrochem. Soc.* **2002**, *149*, A1326–A1331.
[136] S. Komaba, N. Kumagai, Y. Kataoka, *Electrochim. Acta.* **2002**, *47*, 1229–1239.
[137] M. Ochida, Y. Domi, T. Doi, S. Tsubouchi, H. Nakagawa, T. Yamanaka, T. Abe, Z. Ogumi, *J. Electrochem. Soc.* **2012**, *159*, A961–A966.
[138] D. Aurbach, E. Zinigrad, H. Teller, P. Dan, *J. Electrochem. Soc.* **2000**, *147*, 1274–1279.
[139] O. Crowther, A. C. West, *J. Electrochem. Soc.* **2008**, *155*, A806–A811.
[140] R. Bhattacharyya, B. Key, H. Chen, A. S. Best, A. F. Hollenkamp, C. P. Grey, *Nat. Mater.* **2010**, *9*, 504.
[141] Q. Liu, C. Du, B. Shen, P. Zuo, X. Cheng, Y. Ma, G. Yin, Y. Gao, *RSC Adv.* **2016**, *6*, 88683–88700.
[142] D. Aurbach, E. Zinigrad, Y. Cohen, H. Teller, *Solid State Ionics.* **2002**, *148*, 405–416.
[143] T. Ohzuku, T. Yanagawa, M. Kouguchi, A. Ueda, *J. Power Sources.* **1997**, *68*, 131–134.
[144] D. Y. Wan, Z. Y. Fan, Y. X. Dong, E. Baasanjav, H.-B. Jun, B. Jin, E. M. Jin, S. M. Jeong, *J. Nanomater.* **2018**, *1–9*.
[145] K. Min, S.-W. Seo, Y. Y. Song, H. S. Lee, E. Cho, *Phys. Chem. Chem. Phys.* **2017**, *19*, 1762–1769.
[146] C. Pouillerie, L. Croguennec, P. Biensan, P. Willmann, C. Delmas, *J. Electrochem. Soc.* **2000**, *147*, 2061–2069.
[147] C. Pouillerie, F. Perton, P. Biensan, J. P. Pérès, M. Broussely, C. Delmas, *J. Power Sources.* **2001**, *96*, 293–302.
[148] A. Manthiram, J. C. Knight, S. T. Myung, S. M. Oh, Y. K. Sun, *Adv. Energy Mater.* **2016**, *6*, 1501010.
[149] Y. Cho, S. Lee, Y. Lee, T. Hong, J. Cho, *Adv. Energy Mater.* **2011**, *1*, 821–828.
[150] Y. Cho, P. Oh, J. Cho, *Nano Lett.* **2013**, *13*, 1145–1152.
[151] W. Cho, Y. J. Lim, S.-M. Lee, J. H. Kim, J.-H. Song, J.-S. Yu, Y.-J. Kim, M.-S. Park, *ACS Appl. Mater. Interfaces.* **2018**, *10*, 38915–38921.
[152] J. H. Lee, C. S. Yoon, J.-Y. Hwang, S.-J. Kim, F. Maglia, P. Lamp, S.-T. Myung, Y.-K. Sun, *Energy Environ. Sci.* **2016**, *9*, 2152–2158.
[153] B.-B. Lim, S.-J. Yoon, K.-J. Park, C. S. Yoon, S.-J. Kim, J. J. Lee, Y.-K. Sun, *Adv. Funct. Mater.* **2015**, *25*, 4673–4680.
[154] U. H. Kim, E. J. Lee, C. S. Yoon, S. T. Myung, Y. K. Sun, *Adv. Energy Mater.* **2016**, *6*, 1601417.
[155] B.-B. Lim, S.-T. Myung, C. S. Yoon, Y.-K. Sun, *ACS Energy Lett.* **2016**, *1*, 283–289.
[156] Y.-K. Sun, D.-H. Kim, C. S. Yoon, S.-T. Myung, J. Prakash, K. Amine, *Adv. Funct. Mater.* **2010**, *20*, 485–491.
[157] Y.-K. Sun, Z. Chen, H.-J. Noh, D.-J. Lee, H.-G. Jung, Y. Ren, S. Wang, C. S. Yoon, S.-T. Myung, K. Amine, *Nat. Mater.* **2012**, *11*, 942–947.
[158] Z.-D. Huang, X.-M. Liu, B. Zhang, S.-W. Oh, P.-C. Ma, J.-K. Kim, *Scr. Mater.* **2011**, *64*, 122–125.
[159] J. Li, C. Cao, X. Xu, Y. Zhu, R. Yao, *J. Mater. Chem. A.* **2013**, *1*, 11848–11852.
[160] L. Li, L. Wang, X. Zhang, M. Xie, F. Wu, R. Chen, *ACS Appl. Mater. Interfaces.* **2015**, *7*, 21939–21947.
[161] J. Kim, H. Cho, H. Y. Jeong, H. Ma, J. Lee, J. Hwang, M. Park, J. Cho, *Adv. Energy Mater.* **2017**, *7*, 1602559.
[162] J. Cho, T.-J. Kim, Y. J. Kim, B. Park, *Electrochem. Solid-State Lett.* **2001**, *4*, A159–A161.
[163] M. Liang, D. Song, H. Zhang, X. Shi, Q. Wang, L. Zhang, *ACS Appl. Mater. Interfaces.* **2017**, *9*, 38567–38574.
[164] Y. Kim, J. Cho, *J. Electrochem. Soc.* **2007**, *154*, A495-A499.
[165] X. R. Deng, Z. D. Peng, K. Du, *Electrochim. Acta.* **2008**, *53*, 2567.
[166] K. T. Lee, S. Jeong, J. Cho, *Acc. Chem. Res.* **2013**, *46*, 1161–1170.
[167] G.-R. Hu, X.-R. Deng, Z.-D. Peng, K. Du, *Electrochim. Acta.* **2008**, *53*, 2567–2573.
[168] D.-J. Lee, B. Scrosati, Y.-K. Sun, *J. Power Sources.* **2011**, *196*, 7742–7746.
[169] Z. Chen, G.-T. Kim, D. Bresser, T. Diemant, J. Asenbauer, S. Jeong, M. Copley, R. J. Behm, J. Lin, Z. Shen, S. Passerini, *Adv. Energy Mater.* **2018**, *8*, 1870123.
[170] X. Yu, J. B. Bates, G. E. Jellison, F. X. Hart, *J. Electrochem. Soc.* **1997**, *144*, 524–532.
[171] A. T. Appapillai, A. N. Mansour, J. Cho, Y. Shao-Horn, *Chem. Mater.* **2007**, *19*, 5748–5757.
[172] J. Wandt, A. Freiberg, R. Thomas, Y. Gorlin, A. Siebel, R. Jung, H. A. Gasteiger, M. Tromp, *J. Mater. Chem. A.* **2016**, *4*, 18300–18305.

Manuscript received: September 25, 2019
Revised manuscript received: December 30, 2019
Accepted manuscript online: December 30, 2019
Version of record online: February 20, 2020